Rationally Designed Semiconducting 2D Surface-Confined Metal–Organic Network

Vipin Mishra, Showkat H. Mir, Jayant K. Singh,* and Thiruvancheril G. Gopakumar*

ACCESS | Metrics & More | Article Recommendations | SI Supporting Information

ABSTRACT: Two-dimensional (2D) surface-confined metal−organic networks (SMONs) are metal-doped self-assembled monolayers of molecules on solid surfaces. We report the formation of uniform large-area solution-processed semiconducting SMONs of Pd and Zn with mellitic acid (MA) on a highly oriented pyrolytic graphite (HOPG) surface under ambient conditions. The microscopic structure is determined using scanning tunneling microscopy (STM), atomic force microscopy (AFM), and X-ray photoelectron spectroscopy (XPS). Using tunneling spectroscopy, we observed a reduction in the band gap of ≈900 and ≈300 meV for MA−Pd and MA−Zn SMONs, respectively, compared to the pure MA assembly. Concomitant density functional theory (DFT) calculations reveal that the coordination geometry and microscopic arrangement give rise to the observed reduction in the band gap. The dispersion of the frontier bands and their delocalization due to strong electronic coupling (between MA and metal) suggest that the MA−Pd SMON could potentially be a 2D electronic material.

KEYWORDS: 2D molecular material, surface-confined metal−organic network (SMON), electronic structure, scanning tunneling spectroscopy, DFT
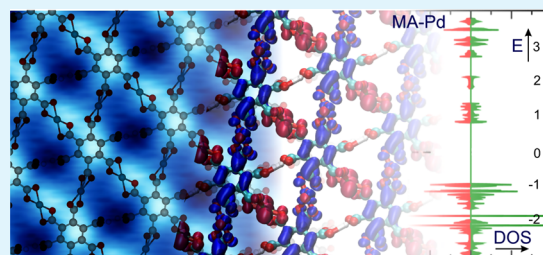
1. INTRODUCTION

There is an increasing demand for two-dimensional (2D) assembly of semiconducting molecules on surfaces due to their potential applications in electronic devices.[1] These 2D assemblies of molecules (or thin film of molecules) are stabilized typically via noncovalent interactions[2] like hydrogen-bonding,[3,4] dipole−dipole,[5,6] and van der Waals interactions.[7] Due to the noncovalent interactions, the electronic coupling between the molecules is weak in their films. Therefore, such films suffer from low charge transport and it limits their application in electronic devices. Typical charge carrier mobility of molecular films is relatively low compared to the inorganic semiconductors; for example, the mobility of well-known semiconducting molecules like pentacene films is 2.2 cm^2/(V s)[8] and that of bisurea derivatives of bithiophene is 5 × 10^{-3} cm^2/(V s).[9] This issue is partly addressed using long aromatic molecules like oligothiophene derivatives and has been explored in optoelectronic applications.[10−12]

Metal doping of molecular thin films could be a possible choice to improve transport in molecular films. Metal doping may be achieved by coordinating the desired molecules with functional groups capable of forming coordination bonds.[13] Due to the strong interaction of ionic/neutral ligand molecules with metal ions, strong electronic coupling is anticipated to improve the charge carrier mobility. In bulk, the electronic properties of coordination polymers have been demonstrated and shown to be suitable for electronic applications.[14−17] Metal doping could be further controlled if the films are

prepared on surfaces, which allows the formation of a two-dimensional (2D) surface-confined metal−organic network (SMON). SMON is particularly interesting as it facilitates the formation of 2D molecular materials. Rational design has been explored to modulate the composition, topology, and function of various SMONs in ultrahigh vacuum on different metal surfaces,[18−25] boron nitride surface,[26] and graphene surface.[27] A semiconducting SMON has also been fabricated based on tetracyanoquinodimethane on a metallic surface.[28] SMONs have also been successfully demonstrated at the solid−liquid interface[29−31] and the solid−air interface.[32]

The carboxyl group has been the focus of several of the above studies for the design of SMON due to its ability to coordinate with metal. To achieve a semiconducting SMON, molecules with a low highest occupied molecular orbital−lowest unoccupied molecular orbital (HOMO−LUMO) gap and predisposed metal coordination sites must be used. We have observed theoretically that mellitic acid (MA) has the lowest HOMO−LUMO gap among the carboxyl-substituted benzene (see the Supporting Information Figure S1 for details) molecules and has been used in the current study in a rational

manner. In this study, we report the formation of uniform large-area semiconducting SMONs of Pd/Zn−mellitic acid on graphite, processed by simple drop-casting from a solution. Compared to the self-assembled adlayer of MA, MA−Pd and MA−Zn SMONs show a substantial reduction in the band gap, with the lowest being for the MA−Pd SMON. Theoretical calculations reveal that the nature of coordination gives rise to the reduced band gap for the MA−Pd SMON.

2. EXPERIMENTAL SECTION

Experimental Details. Mellitic acid (purity ≥99%), anhydrous PdCl$_2$ (purity ≥99.9%), and anhydrous ZnCl$_2$ (purity ≥99.9%) purchased from Sigma Aldrich are used for the experiments with no further purification. The solutions are prepared using methanol (HPLC grade, ≥99.9%) obtained from Merck. Methanolic solution (concentration ≈ 10^{-5} M) of MA and ZnCl$_2$ are mixed and sonicated for 10 min to ensure homogeneous solvation. PdCl$_2$ is sonicated for more than an hour as it is partially soluble in methanol. MA and PdCl$_2$/ZnCl$_2$ are mixed in the ratio 1:2 and drop-cast (≈2 μL) on a freshly cleaved HOPG surface. Agilent-5500 atomic force microscopy (AFM) and RHK STM/Home-built STM are used for analysis under ambient conditions. Imaging is performed both at the solid−air and solid−liquid interfaces (octanoic acid as liquid medium). AFM images are obtained using high-frequency (≈310 kHz, ≈35 N/m) PPP-NCH silicon cantilevers from nanosensors. Mechanically cut Pt/Ir wires are used as STM tips. WSxM[33] software is used for the processing and analysis of all of the AFM and STM data. All voltages in STM data are measured with reference to the sample voltage. dI/dV spectra are measured using a lock-in amplifier. A sine wave with an average voltage of 100 mV (peak to peak) is used for modulation. The obtained dI/dV values on the adlayer and SMONs are normalized with dI/dV obtained on graphite (factored subtraction) to eliminate the strong influence of graphite density of state.[34] To ensure that the solvent does not play a major role in the formation of MA assembly or SMON, we have vacuum-dried (≈0.01 mbar) all of the samples after drop-casting in desiccators for 30 min before scanning. We also note that the microscopic patterns of the MA adlayer and SMONs did not change without pumping, indicating the least influence of solvent on their formation.

Computational Details. Density functional theory (DFT) calculations were performed to study the ground-state properties of the MA adlayer, the MA−Pd SMON, and the MA−Zn SMON using the QUANTUM ESPRESSO package.[35] The electron−ion interaction was described by the Perdew−Burke−Ernzerhof functional with generalized gradient approximation (GGA).[36,37] To obtain the optimized structure, the Kohn−Sham wave functions were expanded by a plane wave basis set with a kinetic energy cutoff of 45 Ry for the wave function and 450 Ry for charge density. Brillouin zone (BZ) integration was done using a uniform Monkhorst−Pack[38] with a k-point grid of 5 × 5 × 1 for geometry optimization and 15 × 15 × 1 for electronic structure calculations. The atomic positions and cell parameters were fully relaxed until an energy convergence of 10^{-8} eV was achieved and the force on each atom was smaller than 0.01 eV/Å. van der Waals interactions were included using DFT−D3[39] dispersion corrections. To avoid the interaction between periodic images, a large vacuum of 20 Å was employed in the z-direction perpendicular to the sheet. To treat the strong on-site Coulomb interaction of localized electrons, which is not correctly described by LDA or GGA, we used Hubbard U correction also for band structure calculations. In our approach, the parameter "U" is defined as the difference between the screened Coulomb and exchange parameters ($U_{eff} = U − J$). The Hubbard parameters 2.0 and 7.5 eV were used for Pd and Zn atoms, respectively.[40,41] All calculations were performed with spin polarization.

3. RESULTS AND DISCUSSION

The carboxyl group in MA promotes both the formation of the adlayer stabilized by hydrogen bonding and metal coordina-

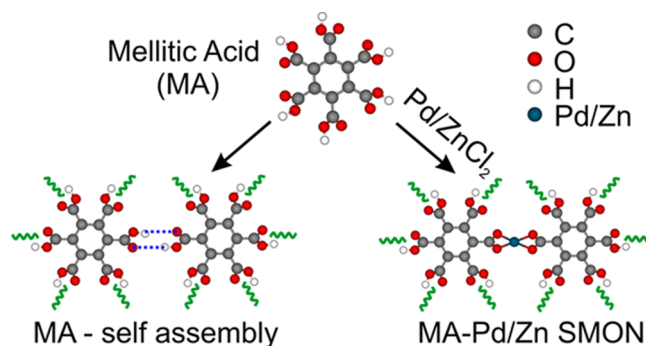tion. Figure 1 shows the schematic of the formation of the hydrogen-bonded (blue dashed lines) adlayer and SMON of

Figure 1. Schematic representation of the formation of a self-assembled adlayer mediated through hydrogen bonding (blue dashed lines) and a metal-coordinated SMON of mellitic acid.

MA with palladium/zinc. Pd/Zn coordinates to the oxygen of carboxyl groups in a square-planar or tetrahedral geometry. The zig−zag lines indicate the 2D extension of adlayer/SMONs. Figure 2a shows a typical AFM phase image of an ultrathin film of MA on HOPG prepared by drop-casting from a methanolic solution (topograph is provided in the Supporting Information Figure S2). We observe islands of MA (indicated by green and magenta dashed lines) with well-defined growth facets uniformly on the HOPG surface. The orientations of the long edge of the molecular islands are indicated using green and magenta arrows and it is observed that they have six typical orientations. This suggests that the molecular lattice of MA is aligned with respect to the graphite lattice. The angle between the green and magenta islands is 9.8 ± 2.7°, which suggests that the long edges of molecular islands are rotated by 4.9° with respect to the graphite compact lattice. The inset of Figure 2a shows a high-resolution image of part of an island. The image is resolved into linelike features (indicated using magenta arrows) that are separated by 1.8 ± 0.2 nm. The distance corresponds to the length of an MA dimer and therefore we suggest that these linelike features most likely correspond to the adjacent molecular rows in the adlayer of MA.

Figure 2b shows the AFM phase image of SMON formed from MA and Pd salt (denoted MA−Pd SMON). The corresponding topograph is provided in the Supporting Information Figure S2. The magenta dashed line indicates an island of the MA−Pd SMON. The nature of the growth is distinctly different from that of the self-assembled MA adlayer. Notably, the average sizes of the SMON islands are relatively larger than the islands of the self-assembled MA adlayer. In addition, these islands also show a preferred orientation of growth on the surface. The orientations of the long edges of the islands are indicated using green and magenta arrows. The angle between the green and magenta islands (7.8 ± 2.7°) is smaller compared to that in the self-assembled MA islands. This indicates that the growth is influenced by the surface and the SMON lattice is rotated by 3.9° with respect to the graphite compact lattice. The inset of Figure 2b shows a high-resolution AFM phase image of part of an island of the MA−Pd SMON. The linelike features (indicated using green arrows) observed in the SMON islands are separated by 6.7 ± 0.3 nm. The spacing between the linelike features indicates that they are originating from a superperiodic pattern of the
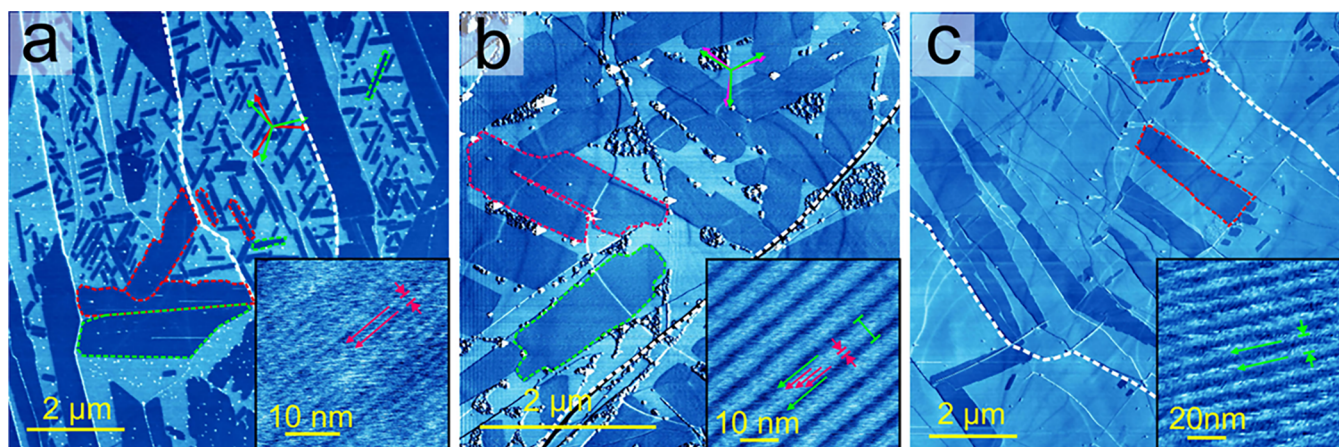
Figure 2. AFM phase image of the ultrathin film of self-assembled MA (a), MA−Pd SMON (b), and MA−Zn SMON (c) on HOPG drop-cast from a methanolic solution. Magenta and green dashed lines show self-assembled molecular and SMON islands (dark contrast) and the bare surface appears light blue. The inset of each image shows the high-resolution AFM phase image of part of an island. Linelike features marked by magenta arrows correspond to adjacent molecular rows in the MA adlayer and the MA−Pd SMON. Green arrows correspond to the superperiodic molecular rows observed in SMON islands. White dashed lines represent a few graphite terraces.
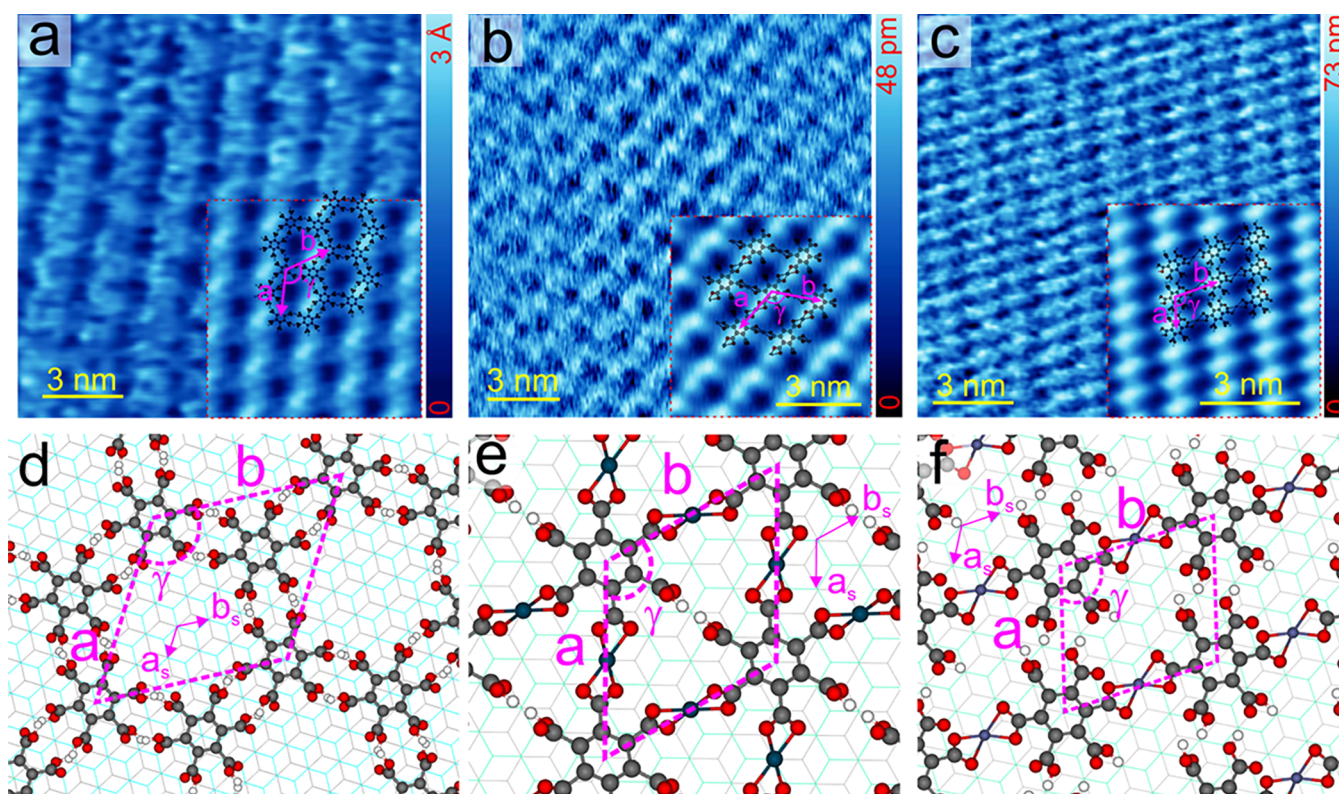

Figure 3. Constant current STM topographs of (a) the MA adlayer (0.50 V, 0.56 nA), (b) the MA−Pd SMON (0.45 V, 0.70 nA), and (c) the MA−Zn SMON (−1.47 V, −0.12 nA). Insets show the mesh-averaged image of the STM topograph. DFT-optimized geometry of the MA chicken-wire (CW) adlayer (d), the MA−Pd SMON (e), and the MA−Zn SMON (f), on bilayer graphite. The graphite layer is shown (below the adlayer/SMON) using cyan and gray hexagonal lattices. a, b, and γ are the lattice parameters of the adlayer and the substrate lattice vectors are a_s and b_s.

MA−Pd SMON most likely originating from a Moiré superpattern. Within the superperiodic pattern, we observed additional linelike features (magenta arrows) that are separated by 1.6 ± 0.3 nm. This corresponds to molecular rows. Figure 2c shows the SMON adlayer formed by MA and Zn salt (denoted as MA−Zn SMON). The growth of the MA−Zn SMON is distinctly different from that of the MA−Pd SMON. The islands of SMON (marked by magenta dashed lines) grow uniformly on the surface; however, they show no preferred

orientation with respect to the surface. The inset shows the high-resolution image of part of an MA−Zn SMON island. Superperiodic patterns are revealed for the MA−Zn SMON and are indicated by green arrows. The spacing between the linelike features is 8.0 ± 1.0 nm. Note that there is no superperiodic pattern for the MA adlayer, suggesting that the molecular lattices are most likely commensurate with the graphite lattice. The apparent heights of the MA adlayer and SMONs as obtained from AFM topographs suggest that the

Table 1. Lattice Parameters (a, b, and γ), Cohesive Energy per Atom, and Band Gap of the MA Adlayer, MA−Pd, and MA−Zn SMONs Obtained Theoretically and Experimentally

molecular system	theory a, b (Å), γ	experimental a, b (Å), γ	E_{coh} (eV/atom)	E_g PBE (eV)	E_g PBE + U (eV)	E_g expt. (eV)
MA−CW[a]	14.96°, 120.0°	15.7 ± 0.4, 115 ± 2°	−6.70	3.69		2.7 ± 0.2
(MA−SF)[a]	(9.99°, 120.0°)		(−6.68)	(2.95)		
MA−Pd[a]	10.11°, 120.0°	11.7 ± 0.5, 119 ± 3°	−6.90	1.76	2.25	1.8 ± 0.2
MA−Zn	8.85°, 9.98°, 106.9°	8.8°, 9.9°, 104 ± 3°	−6.76	2.77	2.85	2.4 ± 0.1

[a]$a \approx$ or $= b$.

islands are monolayered (see the height profiles in the Supporting Information Figure S3).

To understand the microscopic arrangement of MA and Pd/ Zn in the SMONs, we have performed STM experiments. Figure 3 shows the STM topographs (obtained at the HOPG− octanoic acid interface) of ultrathin films of MA (a), MA−Pd (b), and MA−Zn (c) SMONs on HOPG. Large-area STM images are shown in the Supporting Information Figure S4. The ultrathin films of MA−Pd and MA−Zn SMONs are prepared by drop-casting (same as that in the case of AFM studies) and the dried films are further imaged at the HOPG− octanoic acid interface. In the case of MA, molecules were deposited directly from octanoic acid. STM images obtained at the solid−air interface of the drop-cast film of the MA adlayer and SMONs are provided in the Supporting Information Figures S5 and S6. Since the images obtained at the solid−air interface do not provide molecular-level details, we used STM images obtained at the solid−liquid interface for understanding the molecular-level arrangements.

Figure 3a shows the STM topograph of the adlayer of MA at the octanoic acid−HOPG interface. The inset shows an averaged image[42] with $a \approx b$ (15.7 ± 0.4 Å) as unit lattice vectors and γ (115 ± 2°) is the angle between the lattice vectors. The averaged image clearly reveals a porous network pattern similar to that reported for trimesic acid (TMA).[3,43] We tag the assembly as a chicken-wire (CW) pattern. STM images obtained at the solid−air interface reveal linelike contrast separated by ≈16.0 Å that correlates well with the lattice parameters observed at the solid−liquid interface (see the image in the Supporting Information Figure S6). Figure 3d shows a DFT-optimized chicken-wire pattern on bilayer graphite and the lattice parameters are $a = b = 14.96$ Å and $\gamma = 120°$. A commensurate lattice closest to the experimental observation is used as the input. Matrix notation[44] of the unit cell vector for the MA adlayer as per the calculation is given below with substrate lattice vectors a_s, b_s and the adlayer lattice vectors a and b.

$$\begin{bmatrix} a \\ b \end{bmatrix} = \begin{bmatrix} 6 & 0 \\ 0 & 6 \end{bmatrix} \begin{bmatrix} a_s \\ b_s \end{bmatrix}$$

A slightly modified DFT-optimized chicken-wire pattern (for better fit) is overlaid on the averaged STM, which shows the relative orientation of MA molecules within the chicken-wire pattern. The building block of the chicken-wire pattern is the dimer of MA interacting through hydrogen bonding between the carboxyl groups. The center-to-center distance between adjacent MA molecules within the chicken-wire pattern is 9.2 Å and therefore the average hydrogen-bonding distance is 1.68 Å. This corresponds to strong hydrogen bonding as reported for the TMA assembly.[4,45] Unlike in the TMA assembly, the carboxylic groups involved in dimeric hydrogen bonding have a

nearly vertical geometry with respect to the MA plane. This is due to the steric hindrances between the carboxyl groups. This geometry is also seen in the bulk packing of MA.[46] The geometry of the hydrogen-bonded dimeric carboxyl group shows that nearly linear hydrogen bonding is possible between adjacent molecules (the geometry and hydrogen bonding are shown in the Supporting Information Figure S7 using large images).

To determine whether other possible patterns are feasible energetically, we have modeled a possible compact pattern, namely, a superflower (SF) pattern based on trimeric hydrogen bonding (adapted from bulk packing[46]). The corresponding optimized geometry is provided in the Supporting Information Figure S8. The cohesive energy (per molecule) of the CW pattern is 600 meV more compared to that of SF patterns (see Table 1). This suggests that the CW pattern is energetically more favorable than SF on graphite. Therefore, we suggest that the formation of the CW pattern is not influenced by the solid−liquid interface imaging. It is also known for TMA that the dimeric hydrogen-bonded pattern (CW) is favored on graphite over the trimeric hydrogen-bonded SF pattern. It is observed that the CW is preferred both at solid−liquid and solid−air interfaces.[3,4,47]

Figure 3b shows the STM topograph of an MA−Pd SMON (prepared at the HOPG−air interface) imaged at the HOPG− octanoic acid interface. The inset shows an averaged STM image.[42] The unit lattice vectors $a \sim b = 11.7 \pm 0.5$ Å and the angle between the lattice vectors $\gamma = 119 \pm 3°$ are indicated in the image. The lattice parameters and the appearance of the MA−Pd SMON are distinctly different from that of the pure MA adlayer. Interestingly, the magnitudes of lattice vectors along a and b are comparable and are larger than those of a typical MA dimer (center to center). Therefore, we suggest that along a and b the MA molecules are coordinating with Pd through carboxyl groups. Based on the experimental parameters, we have optimized the MA−Pd SMON on bilayer graphite using DFT. The optimized geometry is shown in Figure 3e and the corresponding matrix notation is [5 0, 0 5]. Slightly modified optimized geometry (to fit the STM contrast) is superimposed on the averaged STM image in Figure 3b.

The unit lattice vectors obtained from the calculations (see Table 1) are smaller than the experimental values; however, the angle between the lattices matches very well. We used the nearest possible (compared to experimental a and b) commensurate lattice for the calculations. The overlaid model shows the origin of the STM contrast and the arrangement of MA and Pd within the SMON. Each Pd is coordinated to four oxygen atoms of carboxyl groups of neighboring MA molecules and the coordination geometry is a rectangular plane. The rectangular plane of Pd coordination
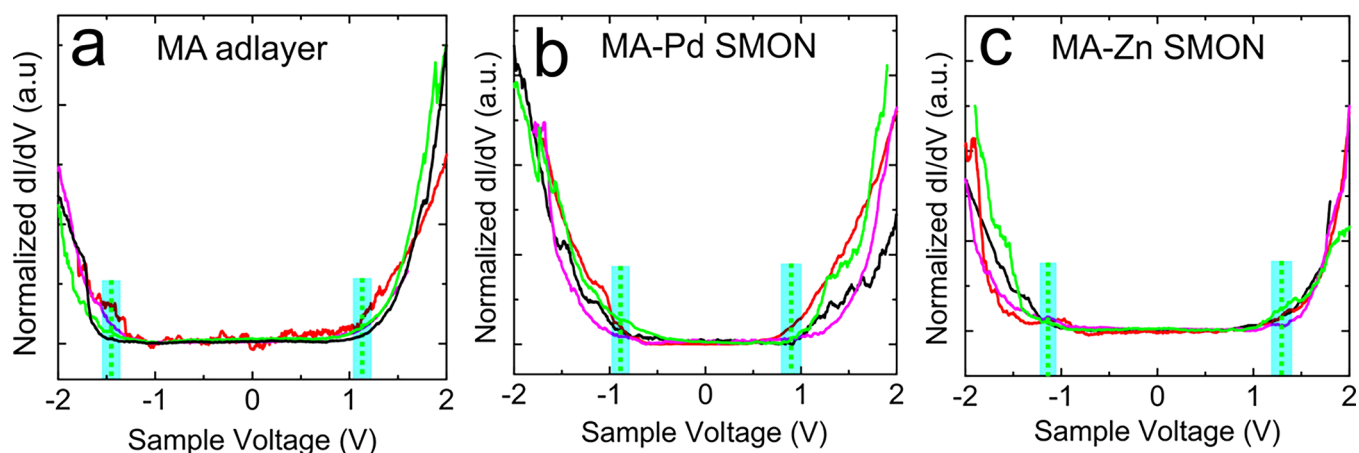
Figure 4. Normalized differential conductance (dI/dV) obtained from the MA adlayer (a), the MA−Pd SMON (b), and the MA−Zn SMON (c). Different colors show different sets of averaged spectra (four sets). Green dashed lines indicate the conduction and valance band edges. All of the STS measurements are performed at the solid−air interface.
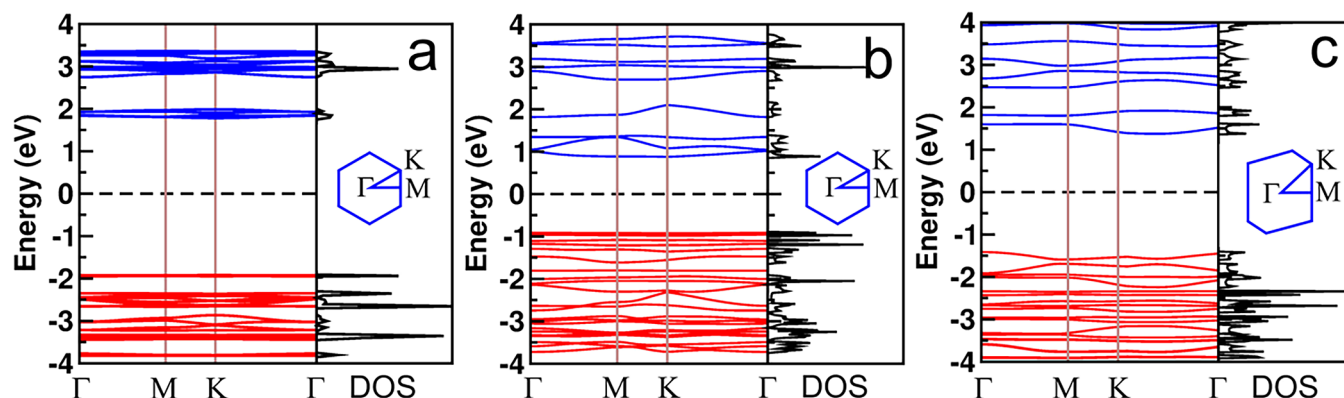

Figure 5. Band structure and the corresponding DOS obtained using DFT calculations for the MA chicken-wire adlayer (a), MA−Pd SMON (b), and MA−Zn SMON (c). Graphite band structure and DOS are excluded.

along a is nearly parallel to the surface plane and that along b is nearly perpendicular to the surface.

Figure 3c shows the STM topograph of an MA−Zn SMON (prepared at the HOPG−air interface) imaged at the HOPG−octanoic acid interface. The inset shows an averaged STM topograph.[42] The unit cell vectors ($a = 8.8 \pm 0.3$, $b = 9.9 \pm 0.6$ Å) and the angle ($\gamma = 104 \pm 3°$) between the vectors of the SMON are indicated in the image. The magnitude of the unit lattice vector along a corresponds to the length of an MA dimer and that along b is larger than the dimer distance. Therefore, we presume that the Zn coordination is asymmetric in the case of the MA−Zn SMON. The angle between the lattice vectors also indicates an asymmetry in the arrangements of molecules within the MA−Zn SMON, unlike in the MA−Pd SMON. To further verify the microscopic arrangement of the MA−Pd SMON, we have performed its DFT optimization on bilayer graphite using the experimental data. The DFT-optimized geometry (see Table 1 for lattice parameters) of the MA−Zn SMON is shown in Figure 3f and the corresponding matrix notation is [4 $\bar{1}$, 0 4]. Slightly modified geometry is overlaid on the mesh-averaged STM topograph (Figure 3c).

The overlaid image clearly shows the microscopic arrangement of MA and Zn within the SMON. The adjacent MA molecules are coordinating with Zn along b and are interacting through dimeric hydrogen bonding along a. We observe six

typical orientations for the islands of the MA−Pd SMON and only three orientations for the MA−Zn SMON (see the Supporting Information Figure S4 for STM images). This suggests that the growth of SMONs is also templated by the symmetry of the surface. To account for the observed Moiré pattern in AFM for MA−Pd and MA−Zn SMONs, we have generated a geometric model of the SMONs on graphite. The geometrical models are well in agreement with the experimentally measured superperiodicity, and details of the model are provided in the Supporting Information Figure S9.

To determine the electronic structure of SMON, we have performed scanning tunneling spectroscopy (STS) at the solid−air interface. Figure 4 shows the normalized differential conductivity (dI/dV) measured on the MA adlayer (Figure 4a) and MA−Pd (Figure 4b) and MA−Zn (Figure 4c) SMONs on HOPG. The dI/dV measured of the MA adlayer and SMONs are normalized using the dI/dV obtained on graphite to reduce the effect of graphite density of state (DOS).[34] Red, black, magenta, and green dI/dV represent averaged independent measurements. The individual normalized dI/dV used for the averaging is shown in the Supporting Information Figures S11−S13 and the averaged raw dI/dV data is shown in the Supporting Information Figure S10. The onset of an increase in the dI/dV signal at a positive sample voltage corresponds to the conduction band edge and that at negative bias corresponds to the valance band edge (zero voltage
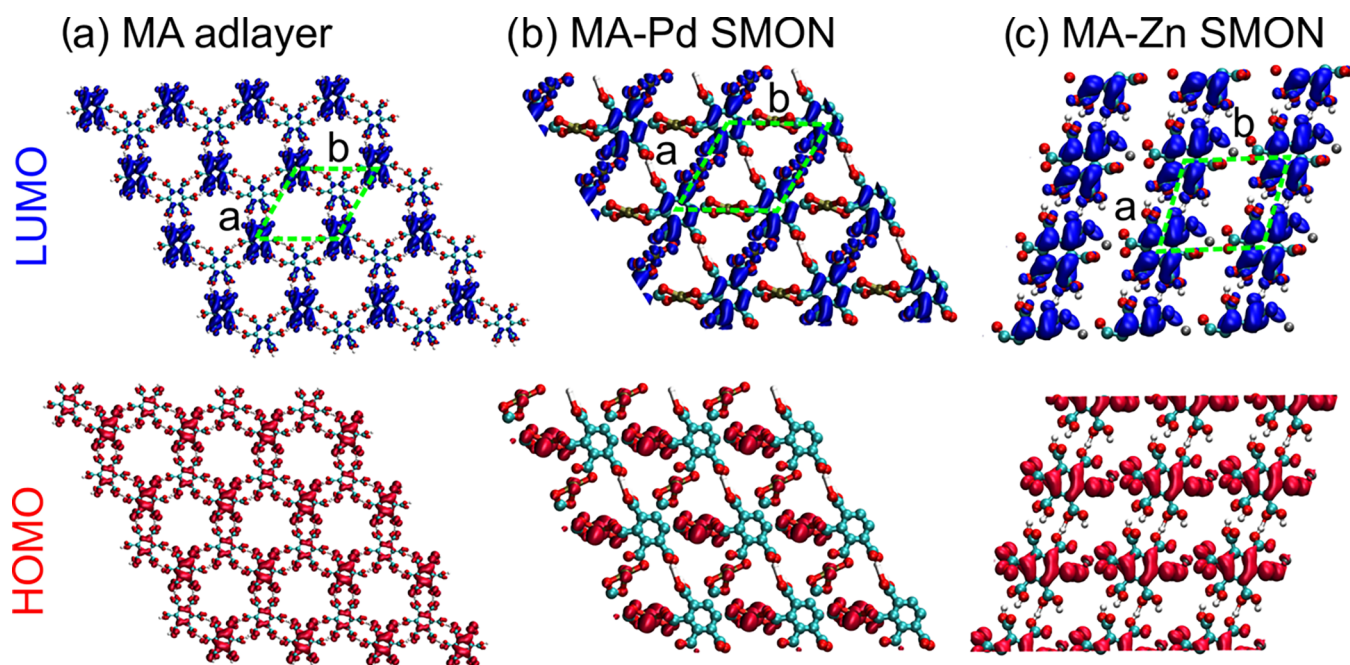
Figure 6. Isosurface plots of HOMO (red) and LUMO (blue) of CW of MA (a), MA−Pd SMON (b), and MA−Zn SMON (c) calculated using the PBE functional. The isosurface values (e/Å^3) are set to 0.000865, 0.000950, and 0.000550 for MA, MA−Pd SMON, and MA−Zn SMON, respectively.

corresponds to the Fermi level). The average onsets are depicted by green dashed lines. The band gap (difference between valance and conduction band edges) of the MA adlayer is 2.7 ± 0.2 eV. Interestingly, the band gaps obtained for both SMON are reduced compared to that of the pure MA adlayer. The band gaps obtained for the MA−Pd SMON and the MA−Zn SMON are 1.8 ± 0.2 and 2.4 ± 0.1 eV, respectively. Particularly, the reduction in the band gap of the MA−Pd SMON is notable as it is reduced by almost 0.9 eV, whereas it is only 0.3 eV for the MA−Zn SMON, compared to that of MA.

We have calculated the density of states (DOS) and band structure of CW and SF patterns of MA and SMONs using DFT to further understand the observed reduction in the band gap of SMONs. Figure 5 shows the calculated band structure and the corresponding DOS of CW of MA (Figure 5a), MA−Pd SMON (Figure 5b), and MA−Zn SMON (Figure 5c). The band structure of MA−SF is shown in the Supporting Information Figure S14. Red and blue lines in the band structure represent the valance band and the conduction band, respectively. The calculated band gaps for CW (SF) of MA, the MA−Pd SMON, and the MA−Zn SMON are 3.69 (2.89), 1.76, and 2.77 eV, respectively, at the PBE level. The calculated band gaps show a clear correlation to the experimentally observed reduction in the band gap of SMONs compared to the MA adlayer. It is particularly noted that the band gap decreases for both SMONs with a notable reduction in the gap for the MA−Pd SMON compared to CW (SF) of MA. The calculated band gaps for MA−Pd and MA−Zn SMONs using Hubbard correction (PBE + U) also show excellent agreement with the experimental result (see the values in Table 1). For the MA−Pd SMON, the band structure obtained using PBE + U is similar to that obtained using PBE and only differs in the band gaps, but for the MA−Zn SMON, there is a slight variation in the band structure (see the Supporting Information Figure S15 for the band structure). The bands

in the conduction and valence bands of CW/SF of MA appear flat as expected for molecular crystals.[48,49] This is due to the weak intermolecular interactions between the MA molecules. Interestingly, for MA−Pd and MA−Zn SMONs, bands near the band edges show reasonable dispersion compared to MA patterns (CW/SF). The dispersion in the bands is attributed to the stronger intermolecular interaction between MA molecules through the Pd/Zn coordination. The strong reduction in the band gap and the dispersion in the band structure of SMONs indicate a strong electronic coupling between MA and Pd/Zn. Spin-polarized DOS values of both SMONs show no asymmetry, indicating that the SMONs have zero magnetic moment. This also indicates that Pd and Zn are in d^8 and d^{10} electronic configurations (closed electronic configurations) in MA−Pd and MA−Zn SMONs, respectively.

We have further analyzed the distribution of electron density corresponding to the frontier bands near the Fermi level of the SMONs. Figure 6 shows the electron density plot of HOMO and LUMO of CW of MA (Figure 6a), MA−Pd SMON (Figure 6b), and MA−Zn SMON (Figure 6c). As expected, the electron density corresponding to both HOMO and LUMO of CW of MA is localized within the region corresponding to molecules. Most strikingly, the electron density corresponding to LUMO of the MA−Pd SMON is delocalized along the compact packing direction *a*. This additionally suggests a strong electronic coupling between MA and Pd in the SMON network. Electron density corresponding to LUMO + 1 also shows a similar behavior (see the details in the Supporting Information Figure S16). In the band structure, the strongest dispersion is also observed for the bands corresponding to LUMO and LUMO + 1. We note that the strongest electronic coupling between MA and Pd is along *a*. This is the compact lattice direction along which the coordination plane of Pd is nearly parallel to the plane of SMON. Thus, the planarity of the coordination of metal with MA along *a* promotes the electronic coupling and therefore the

delocalization of electron density. The HOMO and HOMO − 1 (data in the Supporting Information Figure S16) of the MA−Pd SMON, however, are localized near the metal atoms. We also note that bands corresponding to HOMO and HOMO − 1 show weak dispersion. For the MA−Zn SMON, the electron density corresponding to HOMO and LUMO is localized at the location of MA. However, weaker electronic coupling is clearly observed along the compact packing direction *b*, the direction along which MA is coordinating with Zn. The electronic coupling between MA and Zn is also visible from the dispersed bands near the Fermi level. Electron density plots corresponding to HOMO − 1 and LUMO + 1 are shown in the Supporting Information Figure S16.

We presume that the strong electronic coupling in the MA−Pd SMON is due to the hybridization of d-orbitals of the metal and the π-orbitals of MA owing to the planar geometry of the coordination units within the SMON. While Pd coordination in porphyrin and phthalocyanine molecules shows mixing of metal d-orbitals with π-orbitals in the frontier molecular orbitals, Zn coordination shows weak mixing in the frontier molecular orbitals.[50,51] It is to be noted that the coordination geometry of Pd is planar in porphyrin and phthalocyanine molecules, while the geometry is nonplanar for Zn coordination.[51] In the case of the MA−Zn SMON, Zn is in a tetrahedral geometry and thus the extended electronic coupling is not feasible between the metal d-orbitals and the π-electrons of MA. This electronic coupling has a direct impact on the charge-transport properties of SMON. Since we observed strong dispersion for the unfilled bands, we presume that the MA−Pd SMON may be a suitable electron-transport layer. The strong electronic coupling between MA and Pd in the MA−Pd SMON accounts for the reduction in the band gap compared to that in the MA−Zn SMON.

The calculated cohesive energies of the different SMONs are shown in Table 1 and the MA−Pd SMON shows the highest cohesive energy. Based on the STM and DFT calculations, the number of Pd atoms per unit cell is two in the MA−Pd SMON and one in the MA−Zn SMON. We attribute the high cohesive energy to the strong intermolecular interaction through metal coordination in the MA−Pd SMON.

To confirm and to further understand the coordination geometry of metal in different SMONs, we have investigated isolated metal (Pd/Zn) MA complexes. The optimized geometries of Pd(MA)$_2$ and Zn(MA)$_2$ are shown in Figure 7a,b, respectively. The coordination geometry of Pd is rectangular planar. Further, the average Pd···O bond length is 2.057 Å, which is slightly larger than the reported bond
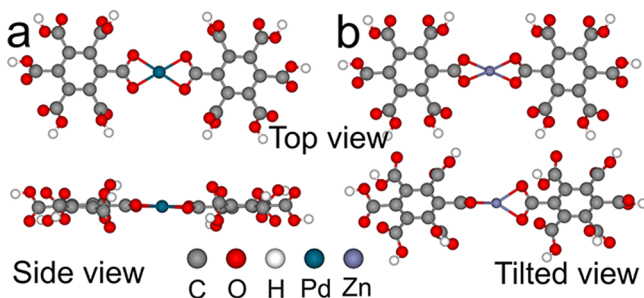
length of Pd···O (1.97−2.01 Å) of several Pd−acetate complexes in their bulk crystals.[52−55] This is most likely due to the relaxed geometry of the Pd(MA)$_2$ complex compared to that in the bulk crystal. When the geometries of isolated complexes are compared to the geometries of Pd(MA)$_2$ units in the MA−Pd SMON, we observe the same rectangular-planar geometry for the Pd coordination. In addition, the Pd···O bond length (2.04 Å) in the MA−Pd SMON is comparable with the bulk crystal structure of Pd−acetate complexes. This suggests that the Pd−MA coordination within the SMON is not geometrically frustrated. This is possibly the reason why the SMON layers grow over several tens of micrometers on the surface without any defects. If there had been restrictions in the coordination, one would have observed smaller domains of SMON.

For the Zn(MA)$_2$ complex, the coordination geometry of Zn reveals a distorted tetrahedral geometry and the average Zn···O distance is 2.03 Å. The geometry of the Zn coordination sphere in the MA−Zn SMON is similar to that obtained in the Zn(MA)$_2$ complex. This shows that the tetrahedral geometry of Zn in the MA−Zn SMON is a geometrically allowed coordination structure and this allows SMON to grow as large domains on HOPG without any geometrical restrictions of coordination. The tetrahedral geometry of Zn in the MA−Zn SMON is also comparable to the tetrahedral coordination geometry of bulk crystals of Zn−acetate complexes.[56,57] The Zn···O distance in Zn−acetate (bulk crystals; 1.94−1.96 Å) and that of the Zn(MA)$_2$ complex are quite comparable. However, the average Zn···O distance in the MA−Zn SMON (2.09 Å) is slightly larger than that in Zn−acetate bulk crystals and Zn(MA)$_2$. This is most likely due to the low packing density of Zn in the MA−Zn SMON (1 Zn per unit cell) compared to Pd in the MA−Pd SMON (2 Pd per unit cell).

Thus, we presume that the planar geometry of the coordination sphere in MA−Pd leads to the observed strong electronic coupling and delocalization of electrons in the SMON network. For the MA−Zn SMON, the tetrahedral geometry is restricting the delocalization of electrons. As per the results obtained from the calculations of isolated complexes, it can be interpreted that the surface plays a minimum role in the coordination geometry. However, the growth propagation is templated by the surface as revealed by the selected orientations of the molecular lattice in the SMONs, thus emphasizing the role of the surface in generating the large-area semiconduction SMONs. Finally, we conclude that the coordination geometry and the electronic configuration of the metal coordination sphere in the SMON are responsible for the tunability of the band gap and the dispersion observed for different bands in the band structure. As shown above, the dispersion in the band structure and the reduction in the band gap give rise to highly delocalized electronic states for the MA−Pd SMON near the Fermi level, which makes it a suitable 2D material for electronic applications. We also propose that if the Pd−MA bulk complex is grown, due to the electron-rich nature of MA and the type of coordination geometry, a semiconducting nature may be expected for the bulk solid.

To further investigate the coordination in SMONs, we have performed X-ray photoelectron spectroscopy (XPS) measurements. Figure 8 shows the O 1s XPS spectra of the MA−Pd SMON (a) and the MA−Zn SMON (b) on HOPG. The graphite C 1s resonance corresponding to sp^2 carbon is used for calibrating the binding energies (BE) of different

Figure 7. DFT-optimized Pd(MA)$_2$ (a) and Zn(MA)$_2$ (b) complexes. Top and side/tilted views are given for the relative view of the coordination sphere. Rectangular-planar and distorted tetrahedral geometries are visible for Pd(MA)$_2$ and Zn(MA)$_2$, respectively.
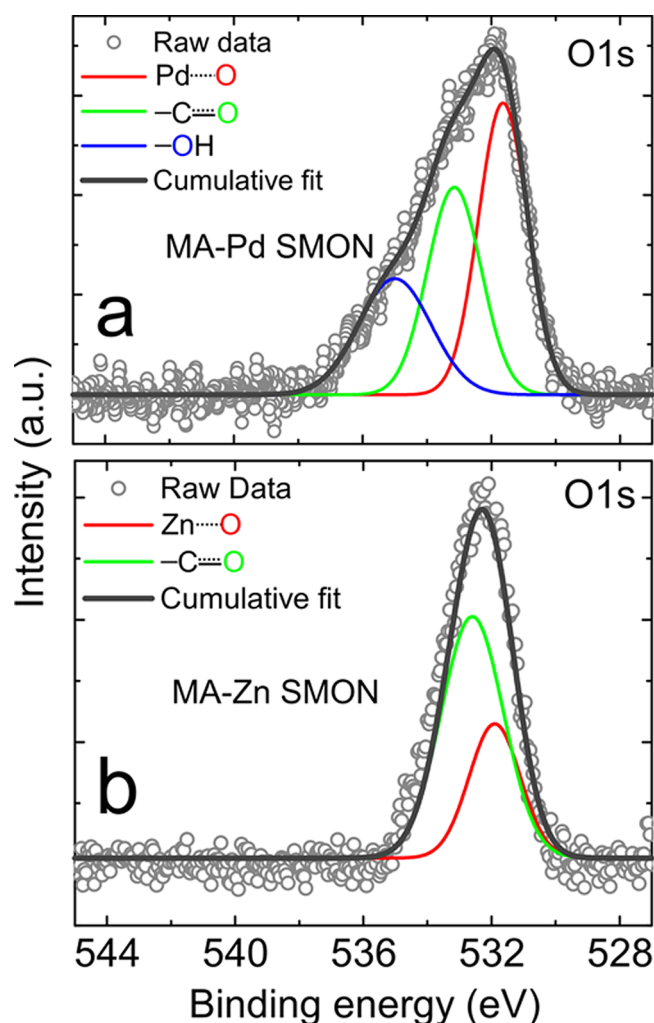
Figure 8. O 1s resonances obtained from XPS measurements of MA−Pd (a) and MA−Zn (b) SMONs on HOPG. Graphite sp^2 resonance is used for the calibration.

resonances. Three O 1s resonances are resolved for the MA−Pd SMON. The resonance observed at 533.15 eV is assigned to hydrogen-bonded oxygen. This assignment is made based on the observation of O 1s resonances in the pure MA adlayer (see the Supporting Information Figure S17). The major O 1s resonance observed for the MA assembly at 532.94 eV corresponds to a hydrogen-bonded C=O/C−O group (or partial double-bonded C and O).[58,59] The major resonance is 532.94 eV and indicates that the majority of the MA molecules form an ordered assembly mediated by dimeric hydrogen bonding of carboxyl groups. The intensity of the resonance corresponding to hydrogen-bonded oxygen (533.15 eV) in the MA−Pd SMON is lower compared to that in the MA assembly (see the Supporting Information Figure S17). This indicates that the number of hydrogen-bonded oxygen decreases in the MA−Pd SMON. The O 1s resonance at 531.64 eV corresponds to the carboxylic oxygen coordinated to Pd and is the intense peak. The BE value of Pd-coordinated oxygen in the MA−Pd SMON agrees with that observed for acetate complexes.[59−61] The high ratio of resonance corresponding to Pd coordinated with oxygen agrees with the expected high number of metal-coordinated oxygen in the MA−Pd SMON. In addition, we observe a broad resonance at higher BE

(535.00 eV), which is attributed to the presence of water or a −OH group.[62]

Figure 8b shows the O 1s resonance of the MA−Zn SMON. The major O 1s resonances are at 531.90 and 532.60 eV, corresponding to oxygen coordinated to Zn[59,62,63] and hydrogen-bonded oxygen,[58,59] respectively. The ratio of the two resonances shows that the percentage of hydrogen-bonded oxygen is higher than that of the metal-coordinated oxygen in MA−Zn SMON. This is in accordance with the microscopic results.

Next, we investigate the changes in metal resonance to understand the nature of coordination (Figure 9). Figure 9a
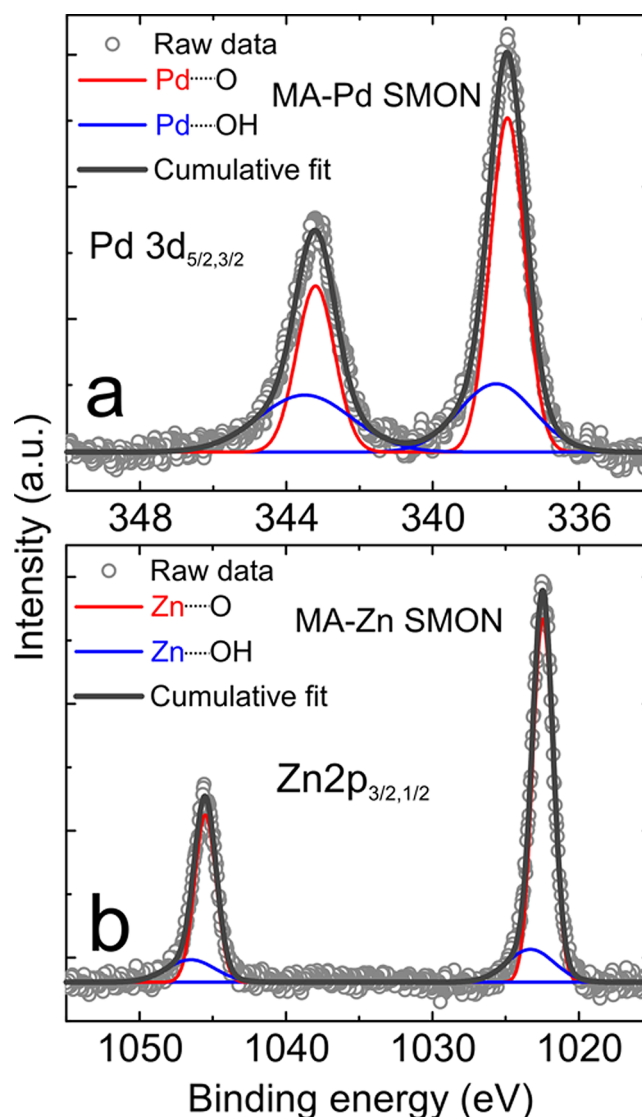

Figure 9. XPS measurements on different SMONs on HOPG. Pd 3d$_{(5/2,3/2)}$ resonances of the MA−Pd SMON (a) and Zn 2p$_{(3/2,1/2)}$ resonances of the MA−Zn SMON (b).

shows the Pd 3d resonances in the MA−Pd SMON. The major peaks at 337.95 (343.20) eV in the MA−Pd SMON correspond to Pd 3d$_{5/2}$ (Pd 3d$_{3/2}$) resonances. The BE of the major peak corresponds to planar (rectangular/square) complexes of Pd, with Pd in a 2+ oxidation state.[60,61,64] The minor peaks at 338.26 (343.49) eV also correspond to Pd(II) and are most likely due to palladium hydroxide.[62] The BE of

Pd $3d_{5/2}$ (Pd $3d_{3/2}$) resonances in the MA−Pd SMON is shifted to be 0.85 eV higher than that of the salt (PdCl$_2$; see the details in the Supporting Information Figure S17). This indicates stronger binding of oxygen with Pd compared to Cl. We attribute this to the chelation of Pd with four oxygen atoms and the compact packing of Pd in SMON. Note that we have observed a similar Pd···O distance in the MA−Pd SMON and that for bulk packing of Pd acetates.[52−55] It is also interesting to note that the full width at half-maximum (FWHM) of the major peak corresponding to Pd $3d_{5/2}$ is reduced by 40% (see the details in Table S1) compared to that in salt. This is most likely related to the regular arrangement of Pd(II) within the SMON, indicating the high and large-area crystallinity of the SMON film. That is, the narrower Pd $3d_{5/2}$ (Pd $3d_{3/2}$) resonances indicate higher monodispersity in the coordination of Pd with MA in an SMON film.

Figure 9b shows the Zn 2p peak in the MA−Zn SMON. The well-defined major peaks at 1022.46 (1045.50) eV in the MA−Zn SMON correspond to Zn $2p_{3/2}$ (Zn $2p_{1/2}$) resonances. Zinc typically shows only a very small shift in the binding energy for the Zn $2p_{3/2}$ (Zn $2p_{1/2}$) region. However, the BE of the observed resonance corresponds to Zn in a 2+ oxidation state.[65] Compared to the Zn $2p_{3/2}$ (Zn $2p_{1/2}$) resonances of salt (ZnCl$_2$; see the details in the Supporting Information Figure S17 and Table S1), the BE is shifted by 0.46 eV to a lower value. Unlike the MA−Pd SMON, the observed downward shift in the BE of Zn $2p_{3/2}$ (Zn $2p_{1/2}$) resonances indicates weaker coordination of Zn with oxygen (Zn−O distance) in the MA−Zn SMON compared to that in the MA−Pd SMON. From the above discussion, it should be noted that the packing density of Zn in the MA−Zn SMON (1 Zn per unit cell) is lower than that compared to Pd in the MA−Pd SMON (2 Pd per unit cell). For Pd in the MA−Pd SMON, we observed an upward shift of BE of Pd $3d_{5/2}$ compared to that in the corresponding salt. Thus, we conclude that the packing density gives rise to strong coordination for Pd (smaller Pd−O distance) in the MA−Pd SMON compared to that for Zn in the MA−Zn SMON. Interestingly, we observe that the FWHM of the major peak corresponding to Zn $2p_{3/2}$ is reduced by 24% compared to that of salt. This is most likely related to the regular arrangement of Zn(II) within the SMON, indicating high and large-area crystallinity of the SMON film similar to that in the MA−Pd SMON. In addition, we observe a minor peak in both the MA−Zn SMON and the Zn salt at 1023.25 eV. This is attributed to the presence of Zn(OH)$_2$ traces in the salt.[66] Note that the BE of the minor peak does not change in the MA−Zn SMON compared to salt, indicating that the Zn(OH)$_2$ present in the salt is not converted into the MA−Zn SMON. This is most likely due to the low coordination ability (reactivity toward a ligand) of carboxyl groups of MA compared to −OH groups in Zn(OH)$_2$. We suggest that the origin of the −OH signal is either due to traces of Pd/Zn(OH)$_2$ in salt or due to the unreacted MA molecules on the surface. In summary, we conclude that the PdCl$_2$/ZnCl$_2$ salt reacts with the carboxyl groups of MA and forms SMONs on graphite in which metal ions (Pd^{2+}/Zn^{2+}) are tetra coordinated with the carboxyl oxygen (M···O) of adjacent MA molecules.

4. CONCLUSIONS

We have successfully prepared large-area domains (≥2 μm) of SMONs of Pd and Zn with mellitic acid on an HOPG surface using a simple drop-casting method. The microscopic structure

and arrangements of SMONs and the MA adlayer are investigated using AFM, STM, and DFT calculations. Further evidence for the formation of metal coordination in SMONs is established using XPS. The electronic properties obtained by tunneling spectroscopy and DFT calculations show a striking reduction in the band gaps of MA−Pd and MA−Zn SMONs compared to the adlayer of MA, with the strongest reduction for the MA−Pd SMON. It is also observed that the electron density of frontier orbitals is delocalized throughout the network for the MA−Pd SMON. The reduction in the band gap and the delocalized electron density is attributed to the nearly planar geometry of the coordination sphere of Pd with the plane of SMON. Thus, the rational design of SMONs particularly with a metal forming a square-planar coordination geometry could be a choice for designing new 2D materials based on molecules for electronic applications.

■ ASSOCIATED CONTENT

ⓈI Supporting Information

The Supporting Information is available free of charge at https://pubs.acs.org/doi/10.1021/acsami.0c16270.

HOMO−LUMO gap of benzene, benzoic acid (BA), trimesic acid (TMA), and mellitic acid (MA) calculated using B3LYP/6-311g implemented in Gaussian 09; AFM topographs and line profiles of MA adlayer and SMONs, STM topograph of the MA adlayer and SMONs obtained at octanoic acid-HOPG and air-HOPG interfaces; single hexagonal unit and hydrogen bonding geometry of the CW pattern of MA; DFT-optimized geometries of a superflower and chicken wire patterns; geometric model for moire pattern; raw dI/dV data; theoretically calculated band structure and density of state of superflower pattern; isosurface plot of HOMO-1, HOMO, LUMO and LUMO+1 of MA adlayer and SMONs and XPS spectra of MA adlayer and Pd/Zn salt (PDF)

■ AUTHOR INFORMATION

Corresponding Authors

Jayant K. Singh − *Department of Chemical Engineering, Indian Institute of Technology Kanpur, Kanpur 208016, India;* orcid.org/0000-0001-8056-2115; Phone: +91 5122596141; Email: jayantks@iitk.ac.in

Thiruvancheril G. Gopakumar − *Department of Chemistry, Indian Institute of Technology Kanpur, Kanpur 208016, India;* orcid.org/0000-0002-3219-7907; Phone: +91 5122596830; Email: gopan@iitk.ac.in; Fax: +91 5122596806

Authors

Vipin Mishra − *Department of Chemistry, Indian Institute of Technology Kanpur, Kanpur 208016, India*

Showkat H. Mir − *Department of Chemistry, Indian Institute of Technology Kanpur, Kanpur 208016, India*

Complete contact information is available at:
https://pubs.acs.org/10.1021/acsami.0c16270

Notes

■ REFERENCES

(1) Mas-Ballesté, R.; Gómez-Navarro, C.; Gómez-Herrero, J.; Zamora, F. 2D Materials: To Graphene and Beyond. *Nanoscale* **2011**, *3*, 20−30.

(2) Whitesides, G. M.; Grzybowski, B. Self-Assembly at All Scales. *Science* **2002**, *295*, 2418−2421.

(3) Griessl, S.; Lackinger, M.; Edelwirth, M.; Hietschold, M.; Heckl, W. M. Self-Assembled Two-Dimensional Molecular Host-Guest Architectures From Trimesic Acid. *Single Mol.* **2002**, *3*, 25−31.

(4) Mishra, V.; Gopakumar, T. G. Comparing Interactions in Threefold Symmetric Molecules at Solid-air Interface. *Surf. Sci.* **2019**, *680*, 11−17.

(5) Müller, D. J.; Sass, H.-J.; Müller, S. A.; Büldt, G.; Engel, A. Surface Structures of Native Bacteriorhodopsin Depend on the Molecular Packing Arrangement in the Membrane. *J. Mol. Biol.* **1999**, *285*, 1903−1909.

(6) Yokoyama, T.; Yokoyama, S.; Kamikado, T.; Okuno, Y.; Mashiko, S. Selective Assembly on a Surface of Supramolecular Aggregates with Controlled Size and Shape. *Nature* **2001**, *413*, 619−621.

(7) Böhringer, M.; Morgenstern, K.; Schneider, W.-D.; Berndt, R.; Mauri, F.; De Vita, A.; Car, R. Two-Dimensional Self-Assembly of Supramolecular Clusters and Chains. *Phys. Rev. Lett.* **1999**, *83*, 324−327.

(8) Jurchescu, O. D.; Popinciuc, M.; van Wees, B. J.; Palstra, T. T. M. Interface-Controlled, High-Mobility Organic Transistors. *Adv. Mater.* **2007**, *19*, 688−692.

(9) Schoonbeek, F. S.; van Esch, J. H.; Wegewijs, B.; Rep, D. B. A.; de Haas, M. P.; Klapwijk, T. M.; Kellogg, R. M.; Feringa, B. L. Efficient Intermolecular Charge Transport in Self-Assembled Fibers of Mono-and Bithiophene Bisurea Compounds. *Angew. Chem., Int. Ed.* **2019**, *38*, 1393−1397.

(10) Mishra, A.; Ma, C.-Q.; Bäuerle, P. Functional Oligothiophenes: Molecular Design for Multidimensional Nanoarchitectures and Their Applications. *Chem. Rev.* **2009**, *109*, 1141−1276.

(11) Kwon, J.; Hong, J.-P.; Noh, S.; Kim, T.-M.; Kim, J.-J.; Lee, C.; Lee, S.; Hong, J.-I. Pyrene End-capped Oligothiophene Derivatives for Organic Thin-film Transistors and Organic Solar Cells. *New J. Chem.* **2012**, *36*, 1813−1818.

(12) Murphy, A. R.; Fréchet, J. M. J.; Chang, P.; Lee, J.; Subramanian, V. Organic Thin Film Transistors from a Soluble Oligothiophene Derivative Containing Thermally Removable Solubilizing Groups. *J. Am. Chem. Soc.* **2004**, *126*, 1596−1597.

(13) Werner, A. Coordination chemistry *Z. Anorg. Chem.* **1893**.

(14) Givaja, G.; Amo-Ochoa, P.; Gómez-García, C. J.; Zamora, F. Electrical Conductive Coordination Polymers. *Chem. Soc. Rev.* **2012**, *41*, 115−147.

(15) Gentili, D.; Givaja, G.; Mas-Ballesté, R.; Azani, M.-R.; Shehu, A.; Leonardi, F.; Mateo-Martí, E.; Greco, P.; Zamora, F.; Cavallini, M. Patterned Conductive Nanostructures from Reversible Self-assembly of 1D Coordination Polymer. *Chem. Sci.* **2012**, *3*, 2047−2051.

(16) Rana, S.; Prasoon, A.; Jha, P. K.; Prathamshetti, A.; Ballav, N. Thermally Driven Resistive Switching in Solution-Processable Thin Films of Coordination Polymers. *J. Phys. Chem. Lett.* **2017**, *8*, 5008−5014.

(17) Rana, S.; Rajendra, R.; Dhara, B.; Jha, P. K.; Ballav, N. Highly Hydrophobic and Chemically Rectifiable Surface-Anchored Metal-Organic Framework Thin-Film Devices. *Adv. Mater. Interfaces* **2019**, *3*, No. 1500738.

(18) Stepanow, S.; Ohmann, R.; Leroy, F.; Lin, N.; Strunskus, T.; Wöll, C.; Kern, K. Rational Design of Two-Dimensional Nanoscale Networks by Electrostatic Interactions at Surfaces. *ACS Nano* **2010**, *4*, 1813−1820.

(19) Álvarez, L.; Peláez, S.; Caillard, R.; Serena, P. A.; Martín-Gago, J. A.; Méndez, J. Metal-organic Extended 2D Structures: Fe-PTCDA on Au(111). *Nanotechnology* **2010**, *21*, No. 305703.

(20) Wäckerlin, C.; Iacovita, C.; Chylarecka, D.; Fesser, P.; Jung, T. A.; Ballav, N. Assembly of 2D ionic layers by reaction of alkali halides with the organic electrophile 7,7,8,8-tetracyano-p-quinodimethane (TCNQ). *Chem. Commun.* **2011**, *47*, 9146−9148.

(21) Abdurakhmanova, N.; Floris, A.; Tseng, T.-C.; Comisso, A.; Stepanow, S.; De Vita, A.; Kern, K. Stereoselectivity and Electrostatics in Charge-Transfer Mn- and Cs- TCNQ4 Networks on Ag(100). *Nat. Commun.* **2012**, *3*, No. 940.

(22) Matena, M.; Björk, J.; Wahl, M.; Lee, T.-L.; Zegenhagen, J.; Gade, L. H.; Jung, T. A.; Persson, M.; Stöhr, M. On-surface Synthesis of a Two-dimensional Porous Coordination Network: Unraveling Adsorbate Interactions. *Phys. Rev. B* **2014**, *90*, No. 125408.

(23) Antczak, G.; Kamiński, W.; Morgenstern, K. Stabilizing CuPc Coordination Networks on Ag(100) by Ag Atoms. *J. Phys. Chem. C* **2015**, *119*, 1442−1450.

(24) Vijayaraghavan, S.; Ecija, D.; Auwärter, W.; Joshi, S.; Seufert, K.; Drach, M.; Nieckarz, D.; Szabelski, P.; Aurisicchio, C.; Bonifazi, D.; Barth, J. V. Supramolecular Assembly of Interfacial Nanoporous Networks with Simultaneous Expression of Metal-Organic and Organic-Bonding Motifs. *Chem. - Eur. J.* **2013**, *19*, 14143−14150.

(25) Bebensee, F.; Svane, K.; Bombis, C.; Masini, F.; Klyatskaya, S.; Besenbacher, F.; Ruben, M.; Hammer, B.; Linderoth, T. R. A Surface Coordination Network Based on Copper Adatom Trimers. *Angew. Chem., Int. Ed.* **2014**, *53*, 12955−12959.

(26) Urgel, J. I.; Schwarz, M.; Garnica, M.; Stassen, D.; Bonifazi, D.; Ecija, D.; Barth, J. V.; Auwärter, W. Controlling Coordination Reactions and Assembly on a Cu(111) Supported Boron Nitride Monolayer. *J. Am. Chem. Soc.* **2015**, *137*, 2420−2423.

(27) Li, J.; Solianyk, L.; Schmidt, N.; Baker, B.; Gottardi, S.; Moreno Lopez, J. C.; Enache, M.; Monjas, L.; van der Vlag, R.; Havenith, R. W. A.; Hirsch, A. K. H.; Stöhr, M. Low-Dimensional Metal-Organic Coordination Structures on Graphene. *J. Phys. Chem. C* **2019**, *123*, 12730−12735.

(28) Shi, X. Q.; Lin, C.; Minot, C.; Tseng, T.-C.; Tait, S. L.; Lin, N.; Zhang, R. Q.; Kern, K.; Cerdá, J. I.; Van Hove, M. A. Structural Analysis and Electronic Properties of Negatively Charged TCNQ: 2D Networks of (TCNQ)2Mn Assembled on Cu(100). *J. Phys. Chem. C* **2010**, *114*, 17197−17204.

(29) De Feyter, S.; Abdel-Mottaleb, M. M. S.; Schuurmans, N.; Verkuijl, B. J. V.; van Esch, J. H.; Feringa, B. L.; De Schryver, F. C. Metal Ion Complexation: A Route to 2D Templates. *Chem. - Eur. J.* **2004**, *10*, 1124−1132.

(30) Kikkawa, Y.; Koyama, E.; Tsuzuki, S.; Fujiwara, K.; Miyake, K.; Tokuhisa, H.; Kanesato, M. Odd-even Effect and Metal Induced Structural Convergence in Self-assembled Monolayers of Bipyridine Derivatives. *Chem. Commun.* **2007**, 1343−1345.

(31) Li, W.; Jin, J.; Leng, X.; Lu, Y.; Liu, X.; Wang, L. Modulation of Coordinate Bonds in Hydrogen-Bonded Trimesic Acid Molecular Networks on Highly Ordered Pyrolytic Graphite Surface. *J. Phys. Chem. C* **2016**, *120*, 12605−12610.

(32) Yadav, K.; Pratibha; Verma, S.; Gopakumar, T. G. Solution-Processed Large-Area Ultrathin Films of Metal-Coordinated Electron-Rich Adenine-Based Ligand. *J. Phys. Chem. C* **2019**, *123*, 20922−20927.

(33) Horcas, I.; Fernández, R.; Gómez-Rodríguez, J. M.; Colchero, J.; Gómez-Herrero, J.; Baro, A. M. WSXM: A Software for Scanning Probe Microscopy and a Tool For Nanotechnology. *Rev. Sci. Instrum.* **2007**, *78*, No. 013705.

(34) Mishra, V.; Yadav, V. K.; Singh, J. K.; Gopakumar, T. G. Electronic Structure of a Semiconducting Imine-Covalent Organic Framework. *Chem. - Asian J.* **2019**, *14*, 4645−4650.

(35) Giannozzi, P.; Baroni, S.; Bonini, N.; Calandra, M.; Car, R.; Cavazzoni, C.; Ceresoli, D.; Chiarotti, G. L.; Cococcioni, M.; Dabo, I.; Dal Corso, A.; de Gironcoli, S.; Fabris, S.; Fratesi, G.; Gebauer, R.; Gerstmann, U.; Gougoussis, C.; Kokalj, A.; Lazzeri, M.; Martin-Samos, L.; Marzari, N.; Mauri, F.; Mazzarello, R.; Paolini, S.; Pasquarello, A.; Paulatto, L.; Sbraccia, C.; Scandolo, S.; Sclauzero, G.; Seitsonen, A. P.; Smogunov, A.; Umari, P.; Wentzcovitch, R. M. QUANTUM ESPRESSO: A Modular and Open-source Software Project for Quantum Simulations of Materials. *J. Phys.: Condens. Matter* **2009**, *21*, No. 395502.

(36) Perdew, J. P.; Burke, K.; Ernzerhof, M. Generalized Gradient Approximation Made Simple. *Phys. Rev. Lett.* **1997**, *78*, 1396.

(37) Perdew, J. P.; Chevary, J. A.; Vosko, S. H.; Jackson, K. A.; Pederson, M. R.; Singh, D. J.; Fiolhais, C. Atoms, Molecules, Solids, and Surfaces: Applications of the Generalized Gradient Approximation for Exchange and Correlation. *Phys. Rev. B* **1992**, *46*, 6671−6687.

(38) Monkhorst, H. J.; Pack, J. D. Special Points for Brillouin-zone Integrations. *Phys. Rev. B* **1976**, *13*, 5188−5192.

(39) Grimme, S.; Antony, J.; Ehrlich, S.; Krieg, H. A Consistent and Accurate Ab initio Parametrization of Density Functional Dispersion Correction (DFT-D) for the 94 Elements H-Pu. *J. Chem. Phys.* **2010**, *132*, No. 154104.

(40) Tang, J.-P.; Wang, L.-L.; Xiao, W.-Z.; Li, X.-F. First Principles Study on Magnetic Properties in ZnS Doped with Palladium. *Eur. Phys. J. B* **2013**, *86*, No. 362.

(41) Yim, K.; Lee, J.; Lee, D.; Lee, M.; Cho, E.; Lee, H. S.; Nahm, H.-H.; Han, S. Property Database for Single-Element Doping in ZnO Obtained by Automated First-Principles Calculations. *Sci. Rep.* **2017**, *7*, No. 40907.

(42) Mesh average: This procedure averages over equivalent parts obtained from an image with periodic contrast. The parts are generated by a 2D FFT of the original image.

(43) Ha, N. T. N.; Gopakumar, T. G.; Hietschold, M. Polymorphs of Trimesic Acid Controlled by Solvent Polarity and Concentration of Solute at Solid-liquid Interface. *Surf. Sci.* **2013**, *607*, 68−73.

(44) Merz, L.; Ernst, K.-H. Unification of the matrix notation in molecular surface science. *Surf. Sci.* **2010**, *604*, 1049−1054.

(45) Steiner, T. The Hydrogen Bond in the Solid State. *Angew. Chem., Int. Ed.* **2002**, *41*, 48−76.

(46) Bezjak, A.; Grdenić, D. Crystal Structure of Mellitic Acid. *Nature* **1960**, *185*, 756−757.

(47) Lackinger, M.; Griessl, S.; Heckl, W. M.; Hietschold, M.; Flynn, G. W. Self-Assembly of Trimesic Acid at the Liquid-Solid Interfacea Study of Solvent-Induced Polymorphism. *Langmuir* **2005**, *21*, 4984−4988.

(48) Droghetti, A.; Rungger, I.; Pemmaraju, C. D.; Sanvito, S. Fundamental gap of molecular crystals via constrained density functional theory. *Phys. Rev. B* **2016**, *93*, No. 195208.

(49) Yanagisawa, S.; Hamada, I. Determination of geometric and electronic structures of organic crystals from first principles: Role of the molecular configuration on the electronic structure. *J. Appl. Phys.* **2017**, *121*, No. 045501.

(50) Gopakumar, T. G.; Meiss, J.; Pouladsaz, D.; Hietschold, M. HOMO-LUMO Gap Shrinking Reveals Tip-Induced Polarization of Molecules in Ultrathin Layers: Tip-Sample Distance-Dependent Scanning Tunneling Spectroscopy on d8 (Ni, Pd, and Pt) Phthalocyanines. *J. Phys. Chem. C* **2008**, *112*, 2529−2537.

(51) Yamashita, K. I.; Hirano, D.; ichi Sugiura, K. Metal Complexes of 5,15-Porphyrinquinones: Systematic Study of Crystal Structure, Electronic Structure and Lewis Acidity. *Eur. J. Inorg. Chem.* **2020**, *2020*, 3507−3516.

(52) Skapski, A. C.; Smart, M. L. The Crystal Structure of Trimeric Palladium(II) acetate. *J. Chem. Soc. D* **1970**, 658b−659.

(53) Stephenson, T. A.; Morehouse, S. M.; Powell, A. R.; Heffer, J. P.; Wilkinson, G. 667. Carboxylates of palladium, platinum, and rhodium, and their adducts. *J. Chem. Soc.* **1965**, 3632−3640.

(54) Bakhmutov, V. I.; Berry, J. F.; Cotton, F. A.; Ibragimov, S.; Murillo, C. A. Non-trivial behavior of palladium(ii) acetate. *Dalton Trans.* **2005**, 1989−1992.

(55) Hamid, M.; Zeller, M.; Hunter, A. D.; Mazhar, M.; Tahir, A. A. Redetermination of bis(2,4-pentanedionato)palladium(II). *Acta Crystallogr., Sect. E: Struct. Rep. Online* **2005**, *61*, m2181−m2183.

(56) Van Niekerk, J. N.; Schoening, F. R. L.; Talbot, J. H. The crystal structure of zinc acetate dihydrate, Zn(CH3COO)2.2H2O. *Acta Crystallogr.* **1953**, *6*, 720−723.

(57) Clegg, W.; Little, I. R.; Straughan, B. P. Monoclinic anhydrous zinc(II) acetate. *Acta Crystallogr., Sect. C: Cryst. Struct. Commun.* **1986**, *42*, 1701−1703.

(58) Lin, N.; Payer, D.; Dmitriev, A.; Strunskus, T.; Wöll, C.; Barth, J. V.; Kern, K. Two-Dimensional Adatom Gas Bestowing Dynamic Heterogeneity on Surfaces. *Angew. Chem., Int. Ed.* **2005**, *44*, 1488−1491.

(59) Sienkiewicz-Gromiuk, J.; Rusinek, I.; Kurach, L.; RzÅczyńska, Z. Thermal and spectroscopic (IR, XPS) properties of lanthanide(III) benzene-1,3,5-triacetate complexes. *J. Therm. Anal. Calorim.* **2016**, *126*, 327−342.

(60) Urbán, B.; Papp, M.; Srankó, D.; Skoda-Földes, R. Phosphine-free atmospheric carbonylation of aryl iodides with aniline derivatives in the presence of a reusable silica-supported palladium catalyst. *J. Mol. Catal. A: Chem.* **2015**, *397*, 150−157.

(61) Bellitto, C.; Bonamico, M.; Fares, V.; Imperatori, P.; Patrizio, S. Tetrathiafulvalenium salts of planar Pt, Pd, and Cu 1,2-dithio-oxalato-S,S' anions. Synthesis, chemistry and molecular structures of bis(tetrathiafulvalenium) bis(1,2-dithio-oxalato-S,S')palladate(II), [ttf]2[Pd(S2C2O2)2], and of bis(tetrathiafulvalenium)-tetrathiafulvalene bis(1,2-dithio-oxalato-S,S')platinate(II), [ttf]3[Pt-(S2C2O2)2]. *J. Chem. Soc., Dalton Trans.* **1989**, 719−727.

(62) Kotsis, K.; Staemmler, V. Ab initio calculations of the O1s XPS spectra of ZnO and Zn oxo compounds. *Phys. Chem. Chem. Phys.* **2006**, *8*, 1490−1498.

(63) Bertoncello, R.; Bettinelli, M.; Casarin, M.; Gulino, A.; Tondello, E.; Vittadini, A. Hexakis(acetato)oxotetrazinc, a well-tailored molecular model of zinc oxide. An experimental and theoretical investigation of the electronic structure of Zn4O(acetate)6 and ZnO by means of UV and X-ray photoelectron spectroscopies and first principle local density molecular cluster calculations. *Inorg. Chem.* **1992**, *31*, 1558−1565.

(64) Zhang, Z.; Hu, H.; Tsi-Yu, K. Poly(styryl)phenanthroline] palladium catalyst. Synthesis and some of its applications in vinylic substitution reactions with organic halides. *React. Polym.* **1988**, *9*, 249−255.

(65) Seals, R. D.; Alexander, R.; Taylor, L. T.; Dillard, J. G. Core electron binding energy study of group IIb-VIIa compounds. *Inorg. Chem.* **1973**, *12*, 2485−2487.

(66) Sharma, A.; Singh, B. P.; Dhar, S. In *Origin of the Green Luminescence Band in ZnO Nanoparticles Synthesized by Sol-Gel Route*, 2011 11th IEEE International Conference on Nanotechnology, 2011; pp 662−665.